Electron Beam Nanosculpting of Kirkendall Oxide Nanochannels

Abdel-Aziz El Mel,[†,∥,*] Leopoldo Molina-Luna,[‡] Marie Buffière,[§] Pierre-Yves Tessier,[∥] Ke Du,[⊥] Chang-Hwan Choi,[⊥] Hans-Joachim Kleebe,[‡] Stephanos Konstantinidis,[†] Carla Bittencourt,[†] and Rony Snyders[†,#]

[†]Chimie des Interactions Plasma-Surface (ChIPS), CIRMAP, Research Institute for Materials Science and Engineering, University of Mons, 23 Place du Parc, B-7000 Mons, Belgium, [‡]Department of Material- and Geosciences, Technische Universität Darmstadt, Schnittspahnstraße 9, 64287 Darmstadt, Germany, [§]imec, Kapeldreef 75, B-3001 Heverlee, Belgium, [∥]Institut des Matériaux Jean Rouxel, Université de Nantes, CNRS, 2 Rue de la Houssinière B.P. 32229, 44322 Nantes Cedex 3, France, [⊥]Department of Mechanical Engineering, Stevens Institute of Technology, Hoboken, New Jersey 07030, United States, and [#]Materia Nova Research Center, 1 Avenue Nicolas Copernic, B-7000 Mons, Belgium

ABSTRACT The nanomanipulation of metal nanoparticles inside oxide nanotubes, synthesized by means of the Kirkendall effect, is demonstrated. In this strategy, a focused electron beam, extracted from a transmission electron microscope source, is used to site-selectively heat the oxide material in order to generate and steer a metal ion diffusion flux inside the nanochannels. The metal ion flux generated inside the tube is a consequence of the reduction of the oxide phase occurring upon exposure to the e-beam. We further show that the directional migration of the metal ions inside the nanotubes can be achieved by locally tuning the chemistry and the morphology of the channel at the nanoscale. This allows sculpting organized metal nanoparticles inside the nanotubes with various sizes, shapes, and periodicities. This nanomanipulation technique is very promising since it enables creating unique nanostructures that, at present, cannot be produced by an alternative classical synthesis route.

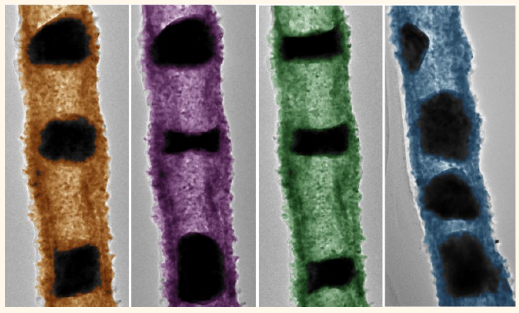

KEYWORDS: nanomanipulation · electron beam · transmission electron microscopy · Kirkendall effect · oxide nanotubes

Ordering nanostructures in a periodic manner is a key to tailoring the properties of materials used in various fields of research including bioscience,[1,2] photonics,[3] and fluidics.[4] Manipulating matter at the nanoscale is a precise block-by-block construction route of novel and periodic low-dimensional systems. This is one of the main reasons driving scientists to push the limits and develop advanced manipulation tools of nanoscopic objects. Some of these tools are based on the plasmonic effect occurring during the exposure of nanoparticles to a light source (*i.e.*, optical tweezers)[5−9] or to an electron beam.[10−12] Other approaches, based on the use of scanning tunneling microscopes[13] or nanoprobes installed on a nanomanipulator in a scanning electron microscope,[14] have also been explored. Since each of these tools has its own limitations, the progress toward the development of new complementary manipulation strategies is still continuing.

Transmission electron microscopy (TEM) is an essential and powerful tool commonly used to analyze nanomaterials. With the substantial developments of electron microscopes and their electron beam (e-beam) sources, new usages of this tool have recently emerged.[15−22] Contrary to what one may expect, irradiating nanostructures with an e-beam may induce several unexpected beneficial effects that allow tailoring of the morphology and structure of the material at the nanoscale.[15−19] For example, electron irradiation was found to induce an extreme pressure increase inside onion-like carbon structures, leading to their transformation into diamond nanoparticles.[15,16] TEM e-beam sources were also used to generate and control vacancies in carbon nanotubes,[20] to weld metal nanowires,[21] and to etch various materials at the nanoscale.[21,22] These successful achievements have proven the technical applicability of TEM e-beam sources as a powerful tool for nanoengineering.

In parallel to the development of electron microscopes, several synthesis methods of hollow nanostructures such as nanoparticles and nanotubes have been reported. Among them, a method based on the nanoscale Kirkendall effect has shown great

* Address correspondence to Abdelaziz.elmel@cnrs-imn.fr.

Received for review December 10, 2013 and accepted January 29, 2014.

Published online January 29, 2014
10.1021/nn406328f

potential in nanoengineering.[23−37] The nanoscale Kirkendall effect describes the displacement of the interface between two different metals due to the unbalanced metal ion interdiffusion fluxes from one side of the interface to another. This in turn induces the injection of vacancies within the fast diffusing material.[32] For some metal nanowires, the Kirkendall effect can occur upon thermal oxidation, leading to their spontaneous transformation into metal oxide nanotubes.[33−36] The stoichiometry (*i.e.*, metal-rich or metal-poor) of the obtained oxide phase can be controlled according to the oxidation conditions.[34] In some particular circumstances, when the self-diffusion (*i.e.*, diffusion of metal in metal) length scale becomes comparable to the diameter of the nanowire, the Kirkendall-induced hollowing-up process can be altered.[34−36] As a consequence, at an intermediate stage of the oxidation process, periodic nanoparticles can be formed inside the metal-oxide nanotubes. The size of the formed particles was reported to be inhomogeneous and their spatial periodicity was very poor due to the isotropic diffusion fluxes of the metal ions inside the tube.[34−36] The noncontrolled random diffusion occurs due to the overall heating of the nano-objects when using a conventional oven.

In order to steer the metal ion diffusion flux toward forming particles with a narrow size distribution and an excellent spatial periodicity, we present a strategy based on site-selective heating and locally tuning the chemistry of the nano-objects using a focused e-beam extracted from a TEM source. Cuprous (Cu_2O) nanotubes, prepared by thermal oxidation of Cu nanowires grown by magnetron sputtering on silicon nanograted structures, were selected as model systems.[21] The proposed method can also be applied to any metal/metal oxide systems in which the Kirkendall effect can take place. The diameter of the Cu nanowires was made large enough to avoid any possible alteration of the Kirkendall-induced hollowing process during oxidation. Specific oxidation conditions, detailed in the Methods section, were selected in order to obtain Cu_2O nanotubes with uniform wall thicknesses (Figure 1a). The formation of such crystalline oxide phase was demonstrated by selected area electron diffraction (SAED) (Figure S1).

RESULTS AND DISCUSSION

Phase Reduction and Generation of Cu Flux. The interaction of the e-beam with the nanotube induces a local increase in the temperature of the material. The reached temperature depends on several parameters such as the electron acceleration voltage, the e-beam spot size, the thermal conductivity of the irradiated material, and the exposure time.[38] In particular, the exposure time is a critical parameter since a continuous exposure to the e-beam leads to an uncontrolled heating process. It is important to mention that to explore the impact of the heating temperature on the nanotubes, a continuous exposure to the e-beam must be applied, whereas exploring the impact of the heating time at a fixed temperature requires a series of short e-beam irradiation shots. In this last case, after each shot the e-beam should be defocused for a period to allow the material to cool and avoid any possible uncontrolled increase in temperature.

At first, the impact of the heating time was explored using a series of repeated e-beam irradiation shots (1 shot = 2 s of e-beam irradiation). The results of this study are summarized in Figure 1. When the e-beam was focused for the first 2 s (1st shot, 1 × 2 s) on the region defined by the yellow circle displayed in Figure 1a, two separate nanoparticles start growing on the inner side of the tube wall (Figure 1b, 1 × 2 s, and d, 1 × 2 s). Each particle consists of assembled single-crystal Cu nanograins (Figure S2). The first particle, P1, was formed at the irradiated region, whereas the second one, P2, appeared about 300 nm away from the irradiation spot. Exposing the same region to another 2 s (2nd shot, 2 × 2 s) led to an increase in the size of both particles. Starting from the third irradiation shot (3 × 2 s), the size of P1 starts decreasing while P2 becomes larger. When reaching the ninth shot (9 × 2 s), P1 disappears and P2 reaches its largest size. In addition to the disappearance of P1 and the growth of P2, a third particle, P3, appears almost at a symmetric position of P2, relative to the irradiated region (Figure 1d, 9 × 2 s). In order to investigate the reversibility of the observed effect, the e-beam was then focused on particle P2 (Figure 1c). After 2 s of irradiation (1 × 2 s), P1 starts appearing once again. When increasing the number of shots on the same region, the size of P2 shrinks and that of P1 increases. After the ninth shot (9 × 2 s), P2 almost disappears and P1 reaches its maximal size. The size of P1 at the final stage (Figure 1c, 9 × 2 s) is smaller than the initial size of P2 (Figure 1b, 9 × 2 s). This result can be attributed to the bulk and surface diffusion of Cu ions (Figure S3) occurring randomly in both directions along the tube axis (Figure 1e). The Cu flux generated inside the tube is expected to be a consequence of the phase reduction of the Cu_2O phase occurring upon exposure to the e-beam. To confirm this assumption, spatially resolved electron energy-loss spectroscopy (EELS) was performed in STEM mode on two different regions of a nanotube (Figure 2a). The first one, assigned as region 1, was not modified by the e-beam, whereas the second one (region 2) covers an area of the nanotube that was exposed to the e-beam until the formation of a nanoparticle. A selection of EELS spectra, recorded from scanning the area shown in region 1, is presented in Figure 2b. For all the spectra, the Cu L_3 and L_2 edges are revealed, and they reflect the typical signature of Cu_2O. Moreover, the Cu L_3/L_2 ratio of the deconvoluted data (*i.e.*, after background subtraction) plotted in Figure 2d are found to be

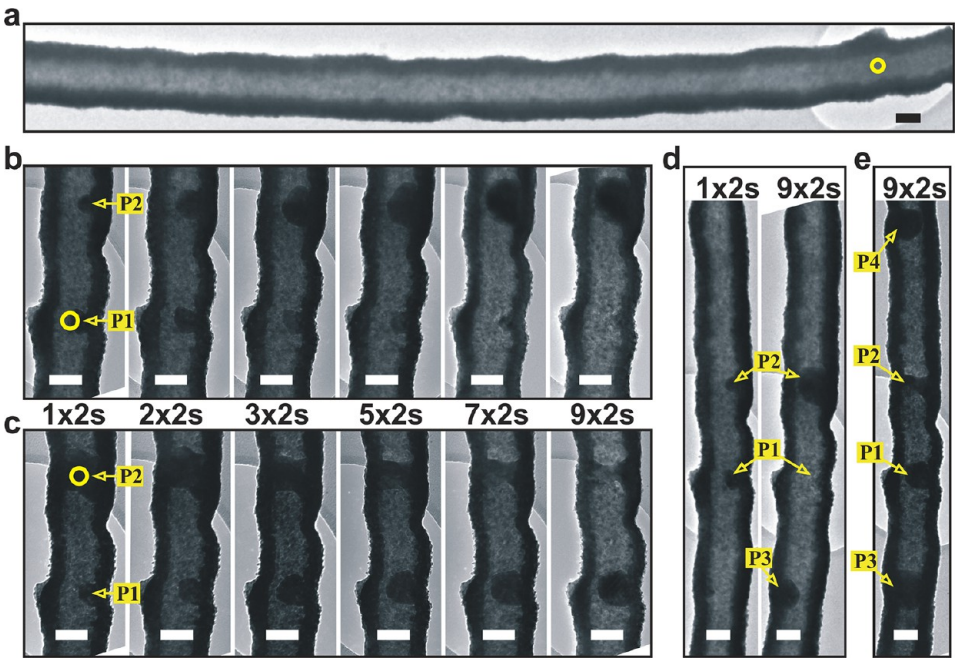

Figure 1. Morphological evolution of an oxide nanotube upon exposure to an electron beam. (a) TEM micrograph of the as-grown oxide nanotube. (b–e) Formation of Cu nanoparticles inside the oxide nanotube upon exposure of several regions to the e-beam for different subsequent shots. The time of each shot was 2 s. The yellow circles indicate the regions irradiated with the e-beam. Scale bar: 100 nm.

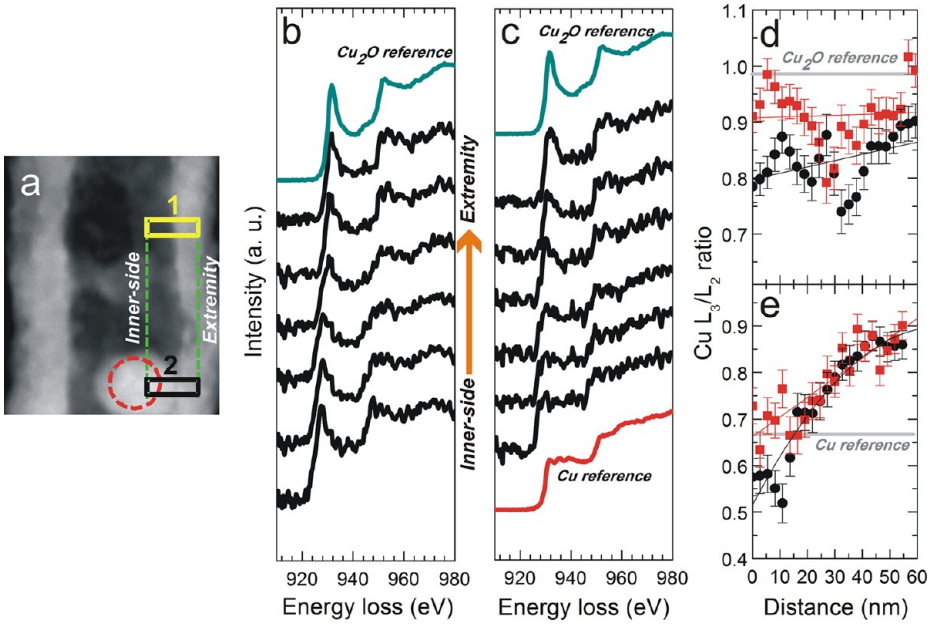

Figure 2. Electron energy-loss spectroscopy showing the impact of the e-beam on the chemical state of an oxide nanotube created by the Kirkendall effect. (a) High-angle annular dark field (HAADF)-STEM micrograph of an oxide nanotube containing a nanoparticle created by irradiation using an e-beam; the dashed red circle represents the e-beam spot, whereas the yellow and the black rectangles represent the two regions analyzed by spatially resolved EELS in combination with STEM. (b) EELS spectra of a hollow tube area composed of cuprous oxide (region 1). (c) EELS spectra of a tube area containing a nanoparticle (region 2); Cu and Cu_2O EELS references are plotted in red and cyan, respectively. (d, e) Evolution of the Cu L_3/L_2 ratios (the raw data are plotted in black, and the deconvoluted ones are in red) on going from the inner side toward the extremity of (d) region 1 and (e) region 2.

almost constant (~0.9) on going from the inner side (*i.e.*, distance = 0 nm) toward the extremity (*i.e.*, distance = 60 nm) of region 1. This result is a direct proof of the unchanged chemical state of the Cu_2O phase in this region. Another behavior was observed in the case of region 2 since the EELS spectra were found to evolve on going from the inner side toward the extremity (Figure 2c). The Cu L_3/L_2 ratio of the deconvoluted data

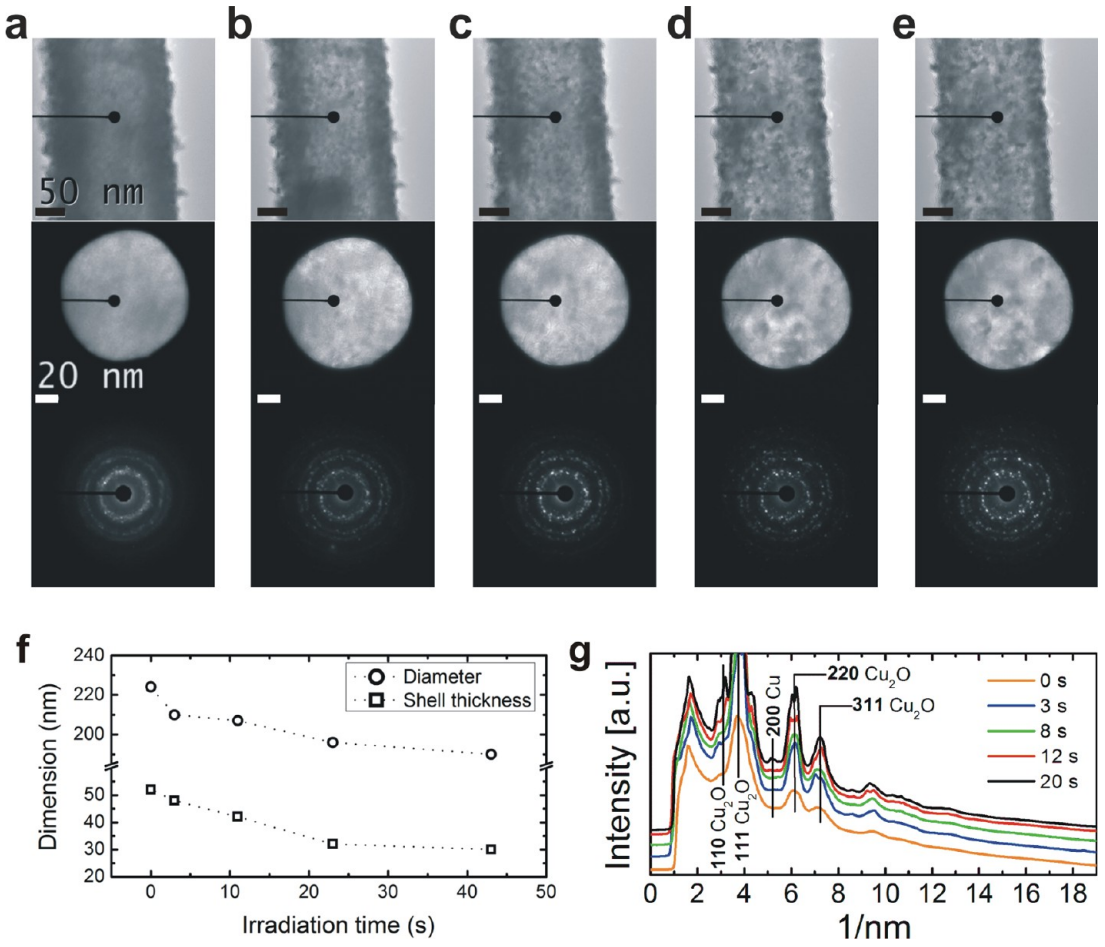

Figure 3. Morphological and structural evolution of a Cu_2O nanotube upon exposure to the e-beam. (a) Initial state before irradiation. (b) After 3 s of exposure. (c) After 8 s of exposure. (d) After 12 s of exposure. (e) After 20 s of exposure. The first row of panels a−e shows the TEM micrographs of the irradiated region. The third and second rows present the SAED patterns and the regions where they were recorded, respectively. The black spots represent the local regions where the e-beam was focused. (f) Evolution of the diameter and the shell thickness as a function of the total irradiation time (*i.e.*, the accumulation of the irradiation time). (g) Rotational average analyses of the SAED patterns displayed in panels a−e.

(Figure 2e) is found to increase from ~0.6 at the inner side until reaching ~0.9 at the extremity. This indicates that while the chemical state of the extremity of the tube at this region stays almost unchanged, the Cu_2O phase at the inner side, directly exposed to the e-beam, undergoes a partial phase reduction. As a consequence, Cu ions migrate randomly inside the nanotube. This isotropic diffusion flux originates from the fact that the diffusion coefficient is identical everywhere inside the tube. Thus, controlling the directional migration of Cu ions requires a local control of their diffusion coefficients, which can be achieved by tuning the chemical state and the morphology of the tube walls.

The control of the chemistry and the morphology of the tube at the nanoscale can be established by continuously irradiating the sample for a long period of time instead of a series of short irradiation shots. Figures 3a−e show a definite region of a nanotube that was irradiated continuously. TEM micrographs and their associated SAED patterns were recorded before and after each irradiation of the same area in order to follow up any possible morphological and structural modification. The increase in the irradiation time results in a decrease in the diameter of the tube and its shell thickness (Figure 3f). This morphological evolution occurs with a structural and chemical modification. Before irradiation (Figure 3a), the electron diffraction reveals the presence of a Cu_2O phase. After 3 s of exposure to the e-beam, a Cu nanoparticle grows inside the tube (Figure 3b). The associated SAED pattern recorded on the irradiated region shows that the tube's shell at this stage is still made of Cu_2O. Irradiating the same area for 8 s more (Figure 3c) followed by 12 s (Figure 3d) leads to an enhancement in the crystalline structure of the Cu_2O phase. Interestingly, the SAED pattern (Figure 3e) recorded after exposing continuously the same region for another 20 s reveals the presence of the 200 diffraction ring of fcc Cu (Figure 3g). The partial transformation of the Cu_2O phase forming the shell into metal Cu proves that the cuprous phase can be partially reduced after a

relatively long and continuous irradiation time. Upon reduction of the Cu_2O phase, oxygen gas was found to be released inside the nanotube, leading to the surface oxidation of the Cu nanoparticles created in the previous stage inside the channel (Figure S4).

Steering the Migration of Cu. Controlling the morphology and the chemistry of the tube by applying a continuous and relatively long exposure to the e-beam further allows steering the diffusion flux of the Cu ions inside the tube. A cuprous nanotube containing two separated metal Cu nanoparticles P1 and P2 is considered in Figure 4a. By focusing the e-beam on the left side of P1 (red circle shown in Figure 4a) a part of the Cu ions will diffuse and leave this irradiated region. As a consequence, the irradiated cuprous region becomes rich in copper and some Cu nanocrystals can be formed in the shell due to the reduction of the Cu_2O phase (Figure 4b). After this stage, P1 will be located between two different oxide regions, where the left one is Cu-rich, thin, and defective and the right one is still made of Cu_2O. The low wall's thickness of the left-hand region will be a limiting factor for the diffusion of the Cu ions. Moreover, the partial reduction of the Cu_2O phase in this region is an additional factor resulting in a low diffusion of Cu through the left-hand side since the diffusion coefficient of Cu ions decreases when increasing the Cu content in a Cu-based oxide phase.[39] Due to these factors, upon exposure of P1 to the e-beam, the Cu ions will diffuse faster in the right-hand region and a Cu track will be created between the particles, in contrast to the left-hand region, where a very small fraction of Cu ions will be able to get through. Thus, the diffusion occurs preferentially toward P2. By implementing this strategy, the diffusion flux of Cu ions can be steered in any required direction in order to create arrays of nanoparticles having well-defined positions and shapes. For the proof of this concept, the nanotube shown in Figure 5a was considered. In a first step, two different separated regions (yellow spots in Figure 5a and b) were irradiated successively in order to produce a set of Cu nanoparticles randomly distributed inside the tube (Figure 5c). Then, the strategy described previously was applied in order to group together the three particles P1, P2, and P3 and form one single particle in the middle of the tube. To do so, the two regions R1 and R2 were successively irradiated, as shown in Figure 5c, for a

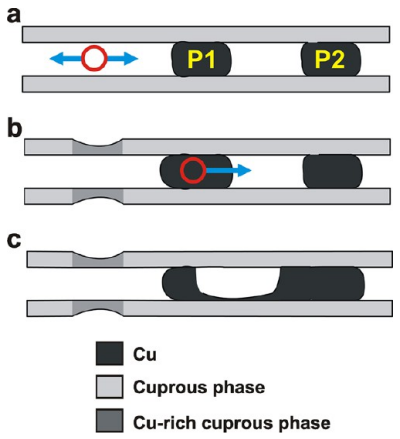

Figure 4. Strategy to control the diffusion of Cu ions inside an oxide nanotube. (a) Oxide nanotube containing two adjacent Cu nanoparticles. (b) Oxide nanotube with a Cu-rich oxide region created by the e-beam. (c) Diffusion of Cu to the right side along the tube axis. The red circles represent the regions irradiated by the e-beam, whereas the blue arrows indicate the diffusion direction of Cu ions.

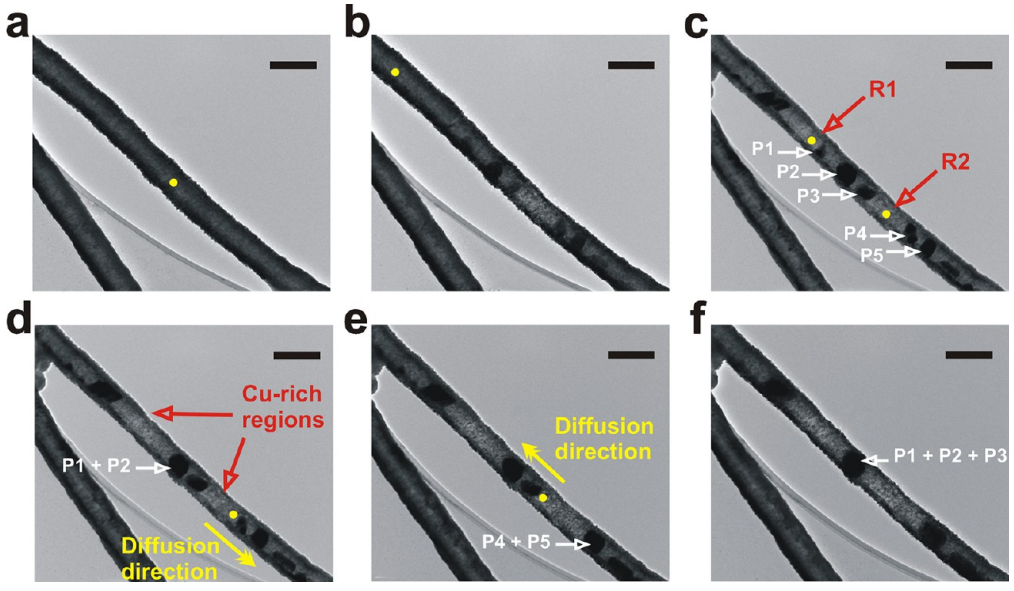

Figure 5. Different transformation stages of a Cu-rich oxide nanotube upon exposure to the e-beam. (a, b) Creation of randomly distributed particles inside the tube. (c–e) Creation of Cu-rich oxide regions and manipulation of Cu particles by the e-beam. (f) Oxide nanotube containing three periodic Cu nanoparticles. Scale bar: 200 nm. The solid yellow dot indicates the position of the e-beam spot.

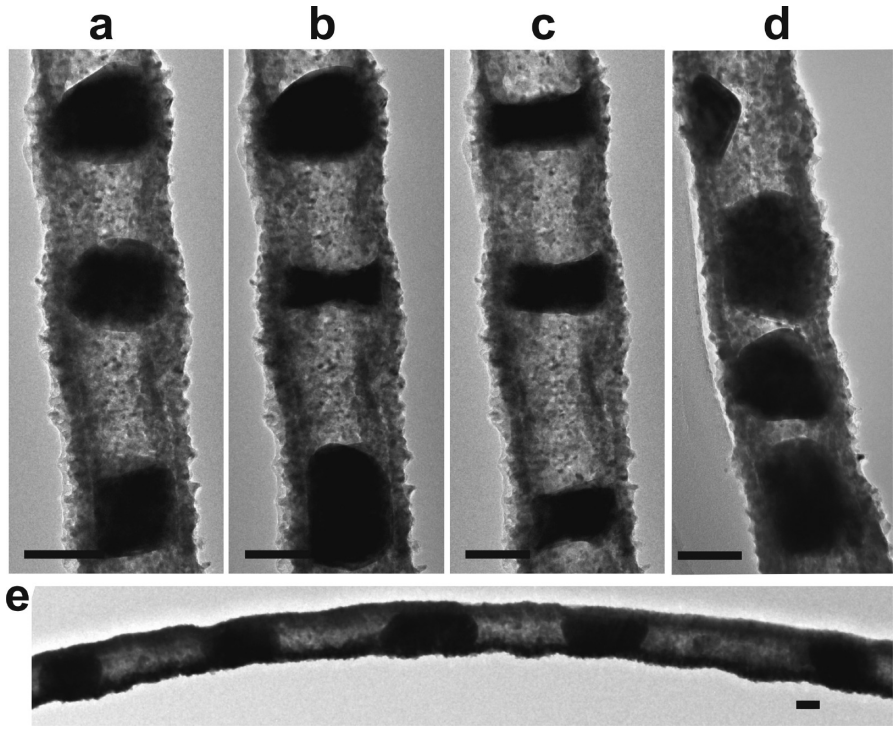

Figure 6. TEM micrographs of various periodic Cu nanostructures created inside an oxide nanotube. (a−c) Creation and sculpting of three periodic particles from a spherical shape to a rectangular one. (d) Periodic spherical nanoparticles with the narrowest separation distance (∼50 nm) that can be obtained before their agglomeration. (e) Cu particles with a large size formed inside the tube over a great length. Scale bar: 100 nm.

period long enough to allow decreasing the thickness of the tube's wall and partially reduce the Cu_2O phase (Figure 5d). When irradiating region R1, P1 was pushed until joining P2. After this stage, the e-beam was placed behind P4 as shown in Figure 5d, in order to group it with P5 (Figure 5e). The same procedure was implemented to combine P3 with the two already agglomerated particles at the center (Figure 5f).

Following the same principle, periodic nanoparticles with smaller separation distances can also be created (Figure 6a). At first, the interstitial space between the upper and the middle particle was exposed briefly to the e-beam in order to partially reduce the oxide phase in this region. Then, by exposing the particle at the middle to the e-beam, it can be sculpted into a smaller particle with a rectangular-like shape (Figure 6b). This size decrease is accompanied by a transformation of the nanoparticle's curved surface from convex (Figure 6a) to concave (Figure 6b). Although the origin of such change is yet not clear, we tentatively associate it with a local modification of the wettability inside the nanotube due to its exposure to the e-beam. This assumption is supported by the recent study of Niu *et al.*, who demonstrated that the wetting properties inside bismuth oxide hollow nanoparticles change during annealing according to several parameters such as the annealing temperature, the variation in the vapor pressure inside the tube, and the diffusion of metal ions on the curved surface of the metal nanoclusters.[37] It should be noted that after this irradiation step the size of the lower particle becomes larger due to the diffused Cu ions. Then, the lower particle was irradiated so as to transform its shape to be rectangular-like. Although the region between the two particles was irradiated in order to reduce the Cu_2O phase, upon irradiation of the lower particle, a part of Cu returns back to the middle one anyway (not shown here). Therefore, in order to efficiently reduce the size of the three particles and sculpt them to rectangular-like shapes as shown in Figure 6c, irradiation steps must be repeated on each particle while surveying the evolution of the particle (*i.e.*, the exposure time requires an adjustment according to the size of the irradiated particle). This additional procedure was not required when the particles were created quite far from each other, as presented previously in Figure 5. Using this additional manipulation procedure, it was also possible to reduce the separation distance between the particles down to ∼50 nm (Figure 5d). However, at such low dimensions the manipulation becomes more delicate and hardly reproducible due to the limitation in size of the used e-beam spot, *e.g.*, ∼50 nm (Figure S5). For smaller separation distances the nanoparticles were found to spontaneously agglomerate. After agglomeration, the formed Cu particle, located between two regions where the Cu_2O phase was reduced, was extremely sensitive to the e-beam. Even a very short irradiation time (∼1 s) could break the

nanotube (Figure S6). When breaking, Cu ions moving from one side to another lead to the formation of a single-crystal nanofilament, bridging the two extremities of the tube. By controlling the time of irradiation, the length of the formed nanofilament can be controlled.

CONCLUSION

In summary, a novel manipulation strategy of Cu nanoparticles inside Kirkendall copper oxide nanotubes has been demonstrated. This strategy is based on the control of the thermally activated local diffusion of Cu ions inside the nanotube using an e-beam extracted from a TEM source. The migration of Cu ions was found to be governed by the surface diffusion mechanism occurring on the inner walls of the nanotube. The directional diffusion of Cu can be achieved by controlling the chemical state of the different regions surrounding the particles. This manipulation technique allows the creation of nanoparticles with various sizes, shapes, and spatial distributions that are confined inside an oxide nanochannel. Copper has been selected as the model system in this study, but this strategy can also be applied to other metals such as iron. In the case of ferromagnetic metals, this nanoscale manipulation strategy could be ideal for the fabrication of novel magnetic nano-objects. The main limitation of the reported nanomanipulation strategy appears to be that it works better for particles with relatively large interparticle distances (>100 nm), limiting the ability to control finely the coupling between magnetic nanoparticles. This limitation is mainly related to the relatively large e-beam spot size (~50 nm) used in this study. One way to overcome this drawback is by decreasing the e-beam spot size, which allows reducing the size of the locally heated area.[21]

METHODS

The Cu-rich oxide nanotubes were synthesized using a two-step strategy that involves the deposition of Cu nanowires on nanograted silicon structures followed by thermal annealing at ambient air. The details concerning this method were reported elsewhere.[21] The nanograted silicon structures were prepared by laser interference lithography followed by deep reactive ion etching.[40,41] For the deposition of Cu nanowires, a copper disk (99.999% pure and 30 mm in diameter) was sputtered in pure argon plasma at a power of 135 W. The distance between the copper target and the substrate was 75 mm. The deposition pressure was fixed to 1.34 Pa, and the deposition time was 2 min. After the growth, the Cu nanowires were thermally oxidized in air using a conventional oven. In order to precisely control the annealing time, gradual heating and cooling were avoided. When the temperature inside the oven stabilizes at 200 °C, the samples were introduced and then immediately taken out after 1 h.

TEM experiments were performed on a JEOL 2100 FEG microscope operating at 200 keV with an emission current of 119 μA. All the irradiation experiments were performed with a magnification of 120 k. When focusing the e-beam, the diameter of the spot was about 50 nm (Figure S4), allowing to reach a current density of 11 pA/cm^2. Rotational average analyses of the electron diffraction data were done using DiffTools (v3.7).[42]

High-angle annular dark field (HAADF)-scanning transmission electron microscopy (STEM) was carried out on a JEOL JEM ARM 200 F (ultra-high-resolution pole piece) operated at 200 kV with a "Schottky" field emission cathode and an aberration-corrector for the probe forming lens, providing a resolution of 0.8 Å in STEM mode and 1.9 Å in TEM mode. A JEOL DF (dark-field) detector and a Gatan digiscan were used for HAADF-STEM imaging.

Spatially resolved electron energy loss spectroscopy in the STEM mode was carried out using a Gatan EFINA detector for spectroscopy and operated at 200 kV. The STEM-EELS area scans were performed using a convergence semiangle α of ~21 mrad and a collection semiangle β of ~100 mrad. All spectra were acquired at an energy dispersion of 0.5 eV/channel and an approximate energy resolution of 1.0 eV. EELS spectra were analyzed using Digital Micrograph, and spatial drift correction was applied. Careful background subtraction was done, and a Fourier-ratio deconvolution was carried out on the spectra to reduce multiple scattering effects originating from the thickness changing of the sample.

Energy dispersive X-ray microanalysis (EDS) was done with a JEOL EDS-system JED-2300T system provided with a 50 mm^2 light-element-sensitive X-ray detector, a digital pulse processor for high-speed accumulation, and a Be double tilt holder. STEM-EDS mapping was performed with JEOL JED-2300 series digital mapping software, and spatial drift correction was applied. A hard X-ray aperture of 200 μm was inserted to avoid stray radiation. Elemental maps were obtained for O−K and Cu−K signals with a resolution of 512 × 512, dwell time of 0.5 ms and a sweep count of 450.

Conflict of Interest: The authors declare no competing financial interest.

Acknowledgment. This work was funded in part by the Directorate of Research in Wallonia, under the scope of the ERA-NET MATERA Programme and by the COST Action MP0901. The French Community of Belgium is acknowledged through the "Cold Plasma" project. S.K. is a research associate of the National Funds for Scientific Research (FNRS, Belgium). The authors gratefully acknowledge I. Wathuthanthri (Stevens Institute of Technology, USA) for help with the laser interference lithography process. The transmission electron microscopes employed for this work were partially funded by the German Research Foundation (DFG).

Supporting Information Available: Crystalline structure of the nanotubes before irradiation as well as that of the nanoparticles created after irradiation. Additional TEM experiments proving the presence of surface diffusion of Cu ions inside the nanotubes. EDS mapping demonstrating the presence of oxygen on the surface of the Cu nanoparticles created inside the nanotubes. Details on the spot size of the used e-beam. A demonstration of a nanotube break-up due to the extreme heating occurring under irradiation. This material is available free of charge *via* the Internet at http://pubs.acs.org.

REFERENCES AND NOTES

1. Frankel, R. B.; Blakemore, R. P.; Wolfe, R. S. Magnetite in Freshwater Magnetotactic Bacteria. *Science* **1979**, *203*, 1355–1356.
2. Mann, S.; Frankel, R. B.; Blakemore, R. P. Structure, Morphology and Crystal Growth of Bacterial Magnetite. *Nature* **1984**, *310*, 405–407.
3. Sun, J.; Timurdogan, E.; Yaacobi, A.; Shah Hosseini, E.; Watts, M. R. Large-Scale Nanophotonic Phased Array. *Nature* **2013**, *493*, 195–199.
4. Xu, W.; Choi, C. H. From Sticky to Slippery Droplets: Dynamics of Contact Line De-pinning on Superhydrophobic Surfaces. *Phy. Rev. Lett.* **2012**, *109*, 024504.

5. Grier, D. G. A Revolution in Optical Manipulation. *Nature* **2003**, *424*, 810–816.
6. Yang, A. H. J.; Moore, S. D.; Schmidt, B. S.; Klug, M.; Lipson, M.; Erickson, D. Optical Manipulation of Nanoparticles and Biomolecules in Sub-wavelength Slot Waveguides. *Nature* **2009**, *457*, 71–75.
7. Grigorenko, A. N.; Roberts, N. W.; Dickinson, M. R.; Zhang, Y. Nanometric Optical Tweezers Based on Nanostructured Substrates. *Nat. Photonics* **2008**, *2*, 365–370.
8. Juan, M. L.; Righini, M.; Quidant, R. Plasmon Nano-Optical Tweezers. *Nat. Photonics* **2011**, *5*, 349–356.
9. Pang, Y.; Gordon, R. Optical Trapping of a Single Protein. *Nano Lett.* **2012**, *12*, 402–406.
10. Batson, P. E.; Reyes-Coronado, A.; Barrera, R. G.; Rivacoba, A.; Echenique, P. M.; Aizpurua, J. Plasmonic Nanobilliards: Controlling Nanoparticle Movement Using Forces Induced by Swift Electrons. *Nano Lett.* **2011**, *11*, 3388–3393.
11. Zheng, H.; Mirsaidov, U. M.; Wang, L. W.; Matsudaira, P. Electron Beam Manipulation of Nanoparticles. *Nano Lett.* **2012**, *12*, 5644–5648.
12. Scholl, J. A.; García-Etxarri, A.; Koh, A. L.; Dionne, J. A. Observation of Quantum Tunneling between Two Plasmonic Nanoparticles. *Nano Lett.* **2013**, *13*, 564–569.
13. Eigler, D. M.; Schweizer, E. K. Positioning Single Atoms with a Scanning Tunneling Microscope. *Nature* **1990**, *344*, 524–526.
14. Peng, Y.; Cullis, T.; Inkson, B. Bottom-Up Nanoconstruction by the Welding of Individual Metallic Nanoobjects Using Nanoscale Solder. *Nano Lett.* **2009**, *9*, 91–96.
15. Banhart, F.; Ajayan, P. M. Carbon Onions as Nanoscopic Pressure Cells for Diamond Formation. *Nature* **1996**, *382*, 433–435.
16. Krasheninnikov, A. V.; Banhart, F. Engineering of Nanostructured Carbon Materials with Electron or Ion Beams. *Nat. Mater.* **2007**, *6*, 723–733.
17. Yang, Y.; Scholz, R.; Berger, A.; Kim, D. S.; Knez, M.; Hesse, D.; Gösele, U.; Zacharias, M. Transmission Electron Microscopy *in Situ* Fabrication of ZnO/Al_2O_3 Composite Nanotubes by Electron-Beam-Irradiation-Induced Local Etching of ZnO/Al_2O_3 Core/Shell Nanowires. *Small* **2008**, *4*, 2112.
18. Wei, X.; Tang, D. M.; Chen, Q.; Bando, Y.; Golberg, D. Local Coulomb Explosion of Boron Nitride Nanotubes under Electron Beam Irradiation. *ACS Nano* **2013**, *7*, 3491–3497.
19. Ran, K.; Zuo, J. M.; Chen, Q.; Shi, Z. Electron Beam Stimulated Molecular Motions. *ACS Nano* **2011**, *5*, 3367–3372.
20. Rodriguez-Manzo, J. A.; Banhart, F. Creation of Individual Vacancies in Carbon Nanotubes by Using an Electron Beam of 1 Å Diameter. *Nano Lett.* **2009**, *9*, 2285–2289.
21. Xu, S.; Tian, M.; Wang, J.; Xu, J.; Redwing, J. M.; Chan, M. H. W. Nanometer-Scale Modification and Welding of Silicon and Metallic Nanowires with a High-Intensity Electron Beam. *Small* **2005**, *1*, 1221–1229.
22. Zheng, K.; Wang, C.; Cheng, Y. Q.; Yue, Y.; Han, X.; Zhang, Z.; Shan, Z.; Mao, S. X.; Ye, M.; Yin, Y.; *et al*. Electron-Beam-Assisted Superplastic Shaping of Nanoscale Amorphous Silica. *Nat. Commun.* **2010**, *1*, 24.
23. Yin, Y.; Rioux, R. M.; Erdonmez, C. K.; Hughes, S.; Somorjai, G. A.; Alivisatos, A. P. Formation of Hollow Nanocrystals through the Nanoscale Kirkendall Effect. *Science* **2004**, *304*, 711.
24. Shevchenko, E. V.; Bodnarchitk, M. I.; Kovalenko, M. V.; Talapin, D. V.; Smith, R. K.; Aloni, S.; Heiss, W.; Alivisatos, A. P. Gold/Iron Oxide Core/Hollow-Shell Nanoparticles. *Adv. Mater.* **2008**, *20*, 4323–4329.
25. Yin, Y. D.; Erdonmez, C. K.; Cabot, A.; Hughes, S.; Alivisatos, A. P. Colloidal Synthesis of Hollow Cobalt Sulfide Nanocrystals. *Adv. Funct. Mater.* **2006**, *16*, 1389–1399.
26. Li, Q.; Penner, R. M. Photoconductive Cadmium Sulfide Hemicylindrical Shell Nanowire Ensembles. *Nano Lett.* **2005**, *5*, 1720–1725.
27. Koo, B.; Xiong, H.; Slater, M. D.; Prakapenka, V. B.; Balasubramanian, M.; Podsiadlo, P.; Johnson, C. S.; Rajh, T.; Shevchenko, E. V. Hollow Iron Oxide Nanoparticles for Application in Lithium Ion Batteries. *Nano Lett.* **2012**, *12*, 2429–2435.
28. Fan, H. J.; Knez, M.; Scholz, R.; Nielsch, K.; Pippel, E.; Hesse, D.; Zacharias, M.; Gosele, U. Monocrystalline Spinel Nanotube Fabrication Based on the Kirkendall Effect. *Nat. Mater.* **2006**, *5*, 627.
29. Fan, H. J.; Knez, M.; Scholz, R.; Hesse, D.; Nielsch, K.; Zacharias, M.; Gosele, U. Influence of Surface Diffusion on the Formation of Hollow Nanostructures Induced by the Kirkendall Effect: The Basic Concept. *Nano Lett.* **2007**, *7*, 993–997.
30. Railsback, J. G.; Johnston-Peck, A. C.; Wang, J.; Tracy, J. B. Size-Dependent Nanoscale Kirkendall Effect during the Oxidation of Nickel Nanoparticles. *ACS Nano* **2010**, *4*, 1913–1920.
31. Yang, Z.; Lisiecki, I.; Walls, M.; Pileni, M. P. Nanocrystallinity and the Ordering of Nanoparticles in Two-Dimensional Superlattices: Controlled Formation of Either Core/Shell (Co/CoO) or Hollow CoO Nanocrystals. *ACS Nano* **2013**, *7*, 1342–1350.
32. Fan, H. J.; Gösele, U.; Zacharias, M. Formation of Nanotubes and Hollow Nanoparticles Based on Kirkendall and Diffusion Processes: A Review. *Small* **2007**, *3*, 1660.
33. El Mel, A. A.; Buffière, M.; Tessier, P. Y.; Konstantinidis, S.; Xu, W.; Du, K.; Wathuthanthri, I.; Choi, C. H.; Bittencourt, C.; Snyders, R. Highly Ordered Hollow Oxide Nanostructures: The Kirkendall Effect at the Nanoscale. *Small* **2013**, *9*, 2838–2843.
34. Nakamura, R.; Matsubayashi, G.; Tsuchiya, H.; Fujimoto, S.; Nakajima, H. Transition in the Nanoporous Structure of Iron Oxides during the Oxidation of Iron Nanoparticles and Nanowires. *Acta Mater.* **2009**, *57*, 4261–4266.
35. Ren, Y.; Chim, W. K.; Chiam, S. Y.; Huang, J. Q.; Pi, C.; Pan, J. S. Formation of Nickel Oxide Nanotubes with Uniform Wall Thickness by Low-Temperature Thermal Oxidation through Understanding the Limiting Effect of Vacancy Diffusion and the Kirkendall Phenomenon. *Adv. Funct. Mater.* **2010**, *20*, 3336–3342.
36. Ren, Y.; Chiam, S. Y.; Chim, W. K. Diameter Dependence of the Void Formation in the Oxidation of Nickel Nanowires. *Nanotechnology* **2011**, *22*, 235606.
37. Niu, K. Y.; Park, J.; Zheng, H.; Alivisatos, A. P. Revealing Bismuth Oxide Hollow Nanoparticle Formation by the Kirkendall Effect. *Nano Lett.* **2013**, *13*, 5715–5719.
38. Egerton, R. F.; Li, P.; Malac, M. Radiation Damage in the TEM and SEM. *Micron* **2004**, *35*, 399–409.
39. Nakamura, R.; Tokozakura, D.; Nakajima, H.; Lee, J. G.; Mori, H. Hollow Oxide Formation by Oxidation of Al and Cu Nanoparticles. *J. Appl. Phys.* **2007**, *101*, 074303.
40. Wathuthanthri, I.; Liu, Y.; Du, K.; Xu, W.; Choi, C.-H. Simple Holographic Patterning for High-Aspect-Ratio Three-Dimensional Nanostructures with Large Coverage Area. *Adv. Funct. Mater.* **2013**, *23*, 608–618.
41. Mao, W.; Wathuthanthri, I.; Choi, C.-H. Tunable Two-Mirror Interference Lithography System for Wafer-Scale Nanopatterning. *Opt. Lett.* **2011**, *36*, 3176–3178.
42. Mitchell, D. R. G. DiffTools: Electron Diffraction Software Tools for DigitalMicrographTM. *Microsc. Res. Tech.* **2008**, *71*, 588–593.